Article

Experimental Study of Accuracy of High-Rate GNSS in Context of Structural Health Monitoring

Xuanyu Qu [1,2], Bao Shu [3,4,*], Xiaoli Ding [1,2], Yangwei Lu [1], Guopeng Li [5] and Li Wang [3,4]

1   Department of Land Surveying and Geo-Informatics, The Hong Kong Polytechnic University, Hong Kong, China
2   Research Institute for Land and Space, The Hong Kong Polytechnic University, Hong Kong, China
3   College of Geological Engineering and Geomatics, Chang'an University, Xi'an 710054, China
4   Key Laboratory of Western China's Mineral Resources and Geological Engineering, Ministry of Education, Xi'an 710054, China
5   The First Geodetic Surveying Bridge of Ministry of Natural Resources, Xi'an 710054, China
*   Correspondence: baos613@chd.edu.cn

Abstract: Global Navigation Satellite Systems (GNSS)-based technologies have become an indispensable part of current structural health monitoring (SHM) systems because of the unique capability of the GNSS technologies to provide accurate real-time displacement information. GNSS equipment with a data sampling rate of up to about 20 Hz has been widely used for this purpose. High-rate GNSS systems (typically up to about 100 Hz) offer additional advantages in structural health monitoring as some highly dynamic civil structures, such as some bridges, require high-rate monitoring data to capture the dynamic behaviors. However, the performance of high-rate GNSS positioning in the context of structural health monitoring is not entirely known, as studies on structural monitoring with high-rate GNSS positioning are very limited, especially considering that some of the satellite systems just reached their full constellations very recently. We carried out a series of experiments with the help of a shaking table to assess the SHM performance of a set of 100 Hz GNSS equipment and three commonly used GNSS positioning techniques, PPP (precise point positioning), PPP-AR (precise point positioning with ambiguity resolution), and RTK (real-time kinematic). We found that the standard deviations of the 100 Hz GNSS displacement solutions derived from PPP, PPP-AR, and RTK techniques were 5.5 mm, 3.6 mm, and 0.8 mm, respectively, when the antenna was in quasi-static motion, and about 9.2 mm, 6.2 mm, and 3.5 mm, respectively, when the antenna was in vibration (up to about 0.7 Hz), under typical urban observational conditions in Hong Kong. We also found that the higher a sampling rate is, the lower the accuracy of a measured displacement series is. On average, the 10 Hz and 100 Hz results are 5.5% and 10.3%, respectively, noisier than the 1 Hz results.

Keywords: high-rate GNSS; structural health monitoring; PPP; PPP-AR; RTK

1. Introduction

Civil engineering structures, such as long-span bridges and tall buildings, are critical components of urban infrastructures. The conditions of these engineering structures are normally monitored closely as they may deteriorate over time, and the loadings may also change due to, e.g., increasing traffic loads on a bridge [1,2]. The failure of an engineering structure may disrupt transport and lead to casualties and economic losses [3]. Global Navigation Satellite Systems (GNSS)-based technologies have been widely used in monitoring displacements of engineering structures and ground motions (e.g., [4,5]). GNSS-based technologies have a distinct advantage in that they are able to provide accurate real-time displacement information. Two main GNSS data processing strategies have been in use in structural health monitoring: real-time kinematic (RTK) positioning and precise point positioning (PPP) [6]. Most of the GNSS positioning errors (e.g., clock errors, orbit errors, and tropospheric and ionospheric effects) can be removed in RTK positioning, resulting in

up to millimeter-level displacement accuracy [7]. The RTK positioning technique has been widely used for monitoring engineering structures, including high-rise buildings, bridges, dams, and wind turbines [8–11]. The accuracy of RTK positioning decreases in general with the length of the baseline [12]. The PPP positioning technique obtains positioning information with a standalone GNSS receiver [13]. Aided with a precise ephemeris, the positioning accuracy of PPP can be up to the centimeter level [14,15]. The technique of PPP with ambiguity resolution (PPP-AR) can further enhance positioning accuracy [16]. PPP and PPP-AR techniques have also been applied in applications such as seismic waveform detection [17]. PPP and PPP-AR have been verified with a low-rate GNSS receiver, a shaking table, and field experiments for monitoring structural displacements [18].

Low data sampling rate GNSS receivers, typically 1–20 Hz, are the mainstream GNSS equipment deployed to date partly due to the wide availability of such GNSS equipment on the market. For example, Yu et al. [19] monitored a bridge using a 1 Hz GPS/GLONASS RTK system to identify the bridge's dynamic characteristics. Moschas et al. [20] evaluated the performance of 10 Hz PPP with the help of a shaking table. Many 10-Hz GNSS RTK systems have been deployed on several real-world long-span bridges, e.g., the Severn suspension bridge in the UK, the Tsing Ma suspension bridge, and the Stonecutters cable-stayed bridge in Hong Kong [21]. However, it is often more desirable to have higher sampling rate data to better define the dynamic characteristics of engineering structures, which may be more suitable for monitoring structures with very high-frequency vibrations, such as the short-span railway bridge, or the bridge with earthquake loading. For example, Cantieni et al. [22] reported that about one-quarter of the railway bridges in Switzerland exhibited natural frequencies above 10 Hz, with some of them reaching about 50 Hz, which is hard to detect based on the GNSS with a normal sampling rate. According to the Nyquist theorem, the Nyquist frequency of GNSS observations should be generally higher than the natural vibration frequency of the structures to avoid aliasing problems. Kaloop et al. [23] indicated that displacement information from very high-rate GNSS was useful for monitoring structural health conditions. Moreover, with the advance in GNSS hardware technologies, the high-sampling rate GNSS receivers (typically 20-100 Hz) have become widely available and emerged as a promising technique for monitoring structural deformation and health assessment. For example, Yi et al. [24] collected 50 Hz GPS data by a JAVAD TRIMMPH-1 receiver to monitor the displacement of a two-floor flexible steel frame model in real-time. Moschas and Stiros [25] used 100 Hz GNSS data (Javad Delta receiver) to study a stiff pedestrian bridge and then analyze the displacement noise characteristics [26]. Paziewski et al. [27] showed that 100 Hz PPP (recorded by Topcon Net-G5 receiver) derived displacements with the help of a filter. In addition, the high-rate GNSS receivers (model: Javad Sigma-G3TAJ) have also successfully been applied in monitoring seismic responses [28,29].

Since studies on high-rate GNSS systems in structural health monitoring are limited, it is not entirely clear how high-rate GNSS systems perform when different positioning techniques are used and different types of displacements are monitored. Although there are some early studies, it still feels necessary to carry out further investigations as some of the satellite constellations have changed. For example, the BeiDou system only reached its full constellation on 23 June 2020 [30]. We aim to evaluate the performance of a high-rate GNSS system when applied for structural health monitoring in a typical urban environment. The study tests the performance of the system when the three most commonly used positioning techniques, i.e., RTK, PPP, and PPP-AR, are used with different sampling rates and with different combinations of the GNSS satellite systems. A uniaxial shaking table and a laser transducer are deployed to simulate different motion signals for the tests. The positioning results are evaluated in both the frequency and time domains.

2. Methods and Materials

2.1. Real-Time Kinematic Positioning

RTK positioning is based on double-differenced (DD) GNSS observations between observational stations and the time to reduce the effects of the spatially correlated errors, such as the ionospheric and tropospheric delays and clock errors, over a short baseline. The DD equations of the pseudorange and carrier-phase observations are [31]

$$P_{br}^{ij,g} = \mu_r^{ij,g} s_r - \rho_{br}^{ij,g} + \delta_P \tag{1}$$

$$\lambda \Phi_{br}^{ij,g} = \mu_r^{ij,g} s_r - \rho_{br}^{ij,g} - \lambda N_{br}^{ij,g} + \delta_\Phi \tag{2}$$

where P and Φ are, respectively, the pseudorange and carrier phase DD observations; δ represents the noise in the pseudorange and carrier phase observations; μ is the LOS (line-of-sight) unit vector from a receiver to a satellite; s is the coordinate components; ρ denotes the geometric distance between the receiver and the satellite; N is the integer phase ambiguity; λ is the wavelength of the carrier phase observations; i and j are the two satellites tracked by both the base (b) and rover (r) stations, where i represents the reference satellite; and superscript g indicates the satellite system, i.e., Global Positioning System (GPS), BeiDou navigation system (BDS), or Galileo and GLONASS. Detailed computation steps for RTK are not given here for brevity. Interested readers may refer to [31].

2.2. Precise Point Positioning

The PPP determines the position of a point with a stand-alone GNSS receiver. With the help of good quality satellite orbit and clock products, the PPP-derived position can reach a centimeter level. Dual-frequency ionospheric-free (IF) pseudorange and carrier phase observations are usually used to reduce the ionospheric effects. After the clock, orbit, and DCB (differential code bias) corrections, the linearized PPP IF observations can be expressed as:

$$\begin{cases} P_{IF}^g = \mu_r^g x + c \cdot \overline{dt}_r^g + T^g + \delta_P \\ \Phi_{IF}^g = \mu_r^g x + c \cdot \overline{dt}_r^g + \overline{N}_{IF}^g + T^g + \delta_\Phi \end{cases} \tag{3}$$

with

$$\begin{cases} c \cdot \overline{dt}_r^g = c \cdot (dt_r^g + \overline{b}_{r,IF}^g / c) \\ \overline{N}_{r,IF}^g = N_{r,IF}^g + \overline{B}_{r,IF}^g - \overline{B}_{IF}^g \end{cases} \tag{4}$$

where P_{IF}^g and Φ_{IF}^g represent the corrected pseudorange and carrier phase observations; c is the speed of light in the vacuum; x is the 3D receiver coordinates; $\overline{dt}_r^g$ and $\overline{N}^g$ denote, respectively, the reformed receiver clock error and phase ambiguity; the slant tropospheric delay is marked as T^g, which contains the hydrostatic delay T_d^g and wet delay T_w^g; $\overline{b}_{r,IF}^g$ is the code hardware bias and grouped into the receiver clock offsets; $\overline{B}_{r,IF}^g$ and $\overline{B}_{IF}^g$ are the receiver and satellite phase hardware biases grouped into the ambiguity parameters, respectively. Based on the assumption that the multi-GNSS code observations share the same receiver clock, the code-specific inter-system bias (ISB) is considered for each system except for GPS.

To obtain a PPP ambiguity resolution, three steps can be followed. First, the fractional cycle biases (FCBs) of the receiver are eliminated by the between-satellite single-difference (BSSD) algorithm [32], while the FCBs of a satellite can be corrected by the WL/NL FCB products or the observable-specific signal bias (OSB) products. The WL float phase ambiguity can be fixed by rounding. Finally, the least-squares ambiguity de-correlation adjustment (LAMBDA) method [33] is adopted to resolve the NL phase ambiguities. When WL and NL ambiguities are fixed, the IF-combined fixed-phase ambiguity can be derived by the following equation.

$$\lambda_{IF} \widetilde{N}_{IF}^g = \frac{c f_2}{f_1^2 - f_2^2} \widetilde{N}_{WL}^g + \frac{c}{f_2 + f_2} \widetilde{N}_{NL}^g \tag{5}$$

where λ_{IF} denotes the wavelength of the IF combined observations; f_1 and f_2 are the frequency of the two-carrier phase; and $\widetilde{N}_{WL}^g$ and $\widetilde{N}_{NL}^g$ represent the WL and NL fixed phase ambiguity in cycles, respectively.

2.3. Experiments

2.3.1. Set Up of Shaking Table

A shaking table test was carried out on the 6th floor of Block Z, The Hong Kong Polytechnic University. Specifically, as shown in Figure 1a, the shaking table was equipped with a GNSS antenna and a MEMS triaxial accelerometer to record the dynamic displacement response of the shaking table. An LDT (Laser Displacement Transducer, model: SENPUM LM-S155) that can record linear displacement at up to 1,000 Hz with an accuracy of 0.01 mm was used to record the true displacement. Another GNSS receiver was set up in an open environment about 100 m away from the shaking table to serve as the base station for the RTK solution, and the location of the base and rover stations is shown in the Figure A1. A GNSS antenna was connected to the data logger (Figure 1c) to synchronize all the sensors to GPS time.
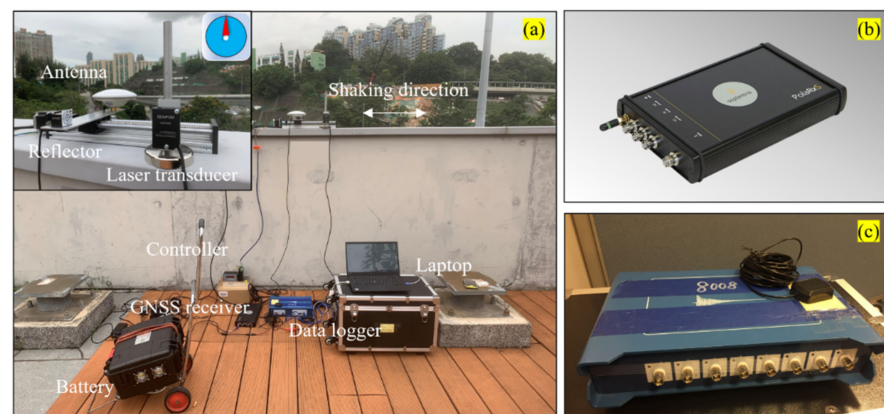
Figure 1. (**a**) Set up of experimental equipment; (**b**) Septentrio GNSS receiver (PolaRx5s) used; and (**c**) data logger with a GPS antenna.

At the start of the experiment, the shaking table remained stationary for over 1 h to obtain the initial coordinates of the antenna. Both dynamic and quasi-static motion signals were then loaded to the shaking table and recorded by the GNSS, accelerometer, and LDT. Specifically, the quasi-static motion (amplitude of about 6 cm) was firstly loaded with very low velocity to avoid possible oscillations. Subsequently, following a short stationary time (about one minute), three sets of sinusoidal motions with different amplitudes and peak frequencies were loaded successively, with a 50-s interval between any two sets.

2.3.2. Data Collection and Processing

Two Septentrio GNSS receivers (model: PolaRx5s, Figure 1b) were used in the experiments to record the GNSS observations at a sampling rate of 100 Hz (for both the rover and base stations). The Septentrio PolaRx5 can track multi-frequency and multi-constellations GNSS signals with 8 logging sessions (more technical parameters can be found at www.septentrio.com). The sampling rate of the LDT was also set to 100 Hz for easy comparison. The Phase Lock Loop bandwidth of the GNSS receiver was set to the default value of 15 Hz. The GNSS data were processed with GPSSHM [34] software and Net_Diff [35] software in RTK, PPP, and PPP-AR modes, respectively. Some details for the data processing are given in Table 1. The final ephemerids and 5-min clock products of the Multi-GNSS Experiment (MGEX) produced by the GeoForschungs Zentrum (GFZ) were used in the PPP processing [36]. The multi-GNSS rapid ephemerides and clock and phase bias products produced by Wuhan University (WUM) were adopted for PPP-AR processing [37]. Four computational schemes based on the different GNSS satellite systems were

adopted. The GPS-only and BeiDou-only solutions were first considered (denoted by 'G' and 'C', respectively). The combined GPS/BeiDou and GPS/BeiDou/Galileo/GLONASS solutions were then computed (denoted by 'GC' and 'GCER', respectively). The accuracies of the estimated displacements were finally evaluated and compared.

Table 1. Details of PPP, PPP-AR, and RTK data processing.

Parameters	PPP	PPP-AR	RTK
Frequency	Dual	Dual	Dual
Sampling rate	0.01s (100 Hz)	0.01s (100 Hz)	0.01s (100 Hz)
Elevation mask	10°	10°	10°
Tropospheric model	Zenith: GPT2w Mapping function: VMF1 [38]	Zenith: GPT2w Mapping function: VMF1 [38]	
Ionospheric model	IF	IF	
Orbit	Final products from GFZ (5 min)	Rapid products from WUM (1 min)	Broadcast ephemerides
Clock	Final products from GFZ (30 s)	Rapid products from WUM (30 s)	Broadcast ephemerids
Estimator	Kalman filter	Kalman filter	Kalman filter

3. Results and Discussion

3.1. Displacement Time Series

The displacement time series computed from the 100-Hz GCER observations are shown in Figure 2. The displacements measured with the LDT (refers to True in Figure 2) are considered the truth and are also shown in the figure for comparison. The time series can be divided into three parts, namely stationary (07:00–08:26), quasi-static (08:26–08:28), and sinusoidal (08:28–08:38) motions. The first part also includes the time for the PPP convergence. The quasi-static motion simulated permanent deformation and the sinusoidal motion may correspond to vibrations.
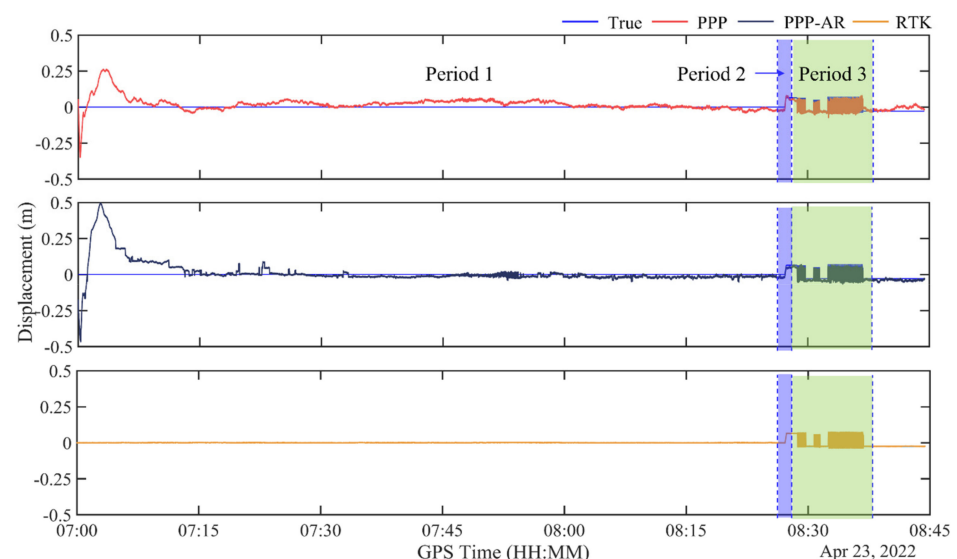
Figure 2. Displacement time series computed from the GCER observations and (top) PPP, (middle) PPP-AR, and (bottom) RTK methods.

Figures 2a and 2b show that the PPP and PPP-AR solutions took about 15 min to converge to a centimeter level. After that, the PPP, PPP-AR, and RTK techniques all captured both the stationary and dynamic displacement signals well. In general, as expected, the RTK solutions are the best. The PPP-AR and PPP results show a sub-centimeter to centimeter-

level accuracy. Further analysis of the performance of the ultra-high-rate GNSS will be given in the following sub-sections.

3.2. Evaluation of Accuracy of the 100-Hz Displacement Time Series

3.2.1. Stationary Test

We first compared the 3D displacement results during the stationary period to study the noise level of different displacement time series computed with the PPP, PPP-AR, and RTK techniques based on different GNSS observations. The standard deviations (STDs) are calculated for quantifying the noise level of displacement and labeled in Figure 3. As depicted in Figure 3, the RTK displacement time series show more stability, followed by the PPP-AR solutions. Apparent oscillations can be observed in the displacement time series derived by the PPP technique, especially for upward direction, with the STDs being at 6.98 cm, 5.32 cm, 4.03 cm, and 2.92 cm for G, C, GC, and GCER observations, respectively. For all three positioning techniques, the GPS-only solutions have the highest noise level with STD values of up to 6.98 cm, 5.38 cm, and 0.60 cm for the PPP, PPP-AR, and RTK techniques, respectively. The main reason is that the limited GPS satellites are tracked during the experiment (about 5 G, Figure A1). With more satellite observations involved, the other three solutions (C, GC, GCER) show an improvement of up to 75% compared to the GPS-only solutions. When using four GNSS system observations, the RTK solutions can achieve a millimeter-level accuracy of 3D displacement (STD = 0.10 cm, 0.09 cm, and 0.22 cm for E, N, and U, respectively), followed by the PPP-AR that allowed millimeter-level accuracy in the horizontal direction and centimeter-level in the vertical direction.
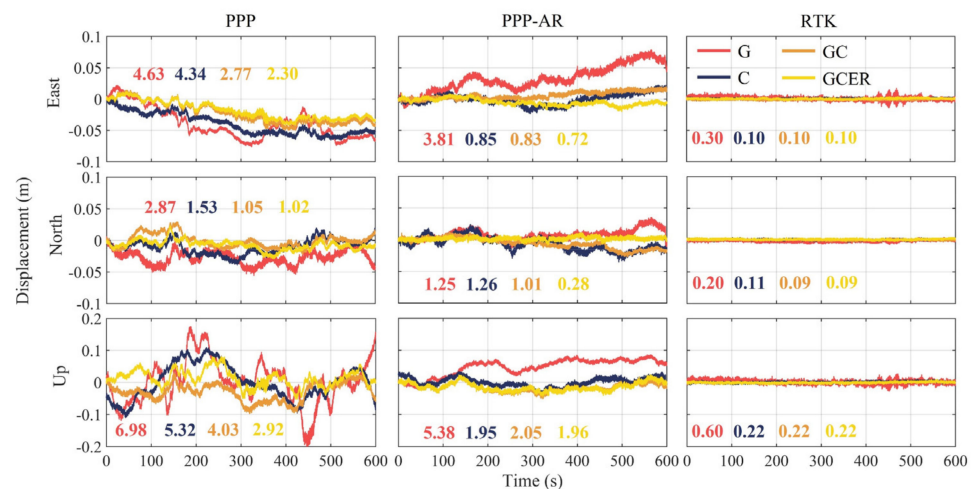
Figure 3. 100-Hz 3D displacement time series from G, C, GC, and GCER observations, respectively, and PPP, PPP-AR, and RTK techniques. The upper, middle, and lower panels represent displacements in the East, North, and Up directions, respectively, while the left, middle, and right columns represent results from PPP, PPP-AR, and RTK, respectively. The standard deviation (in cm) of each time series is given in the corresponding color.

We also calculated the amplitude spectra of the displacement for the stationary test calculated by the Fast Fourier Transform (FFT) to identify the noise spectral characteristics, shown in Figure 4. According to the FFT results of the background noise analysis, more significant attenuation of the noise level can be found in the RTK-derived displacement solutions, especially for using the GCER observations. In the low-frequency band, results computed with GCER show better performance for all three positioning techniques.
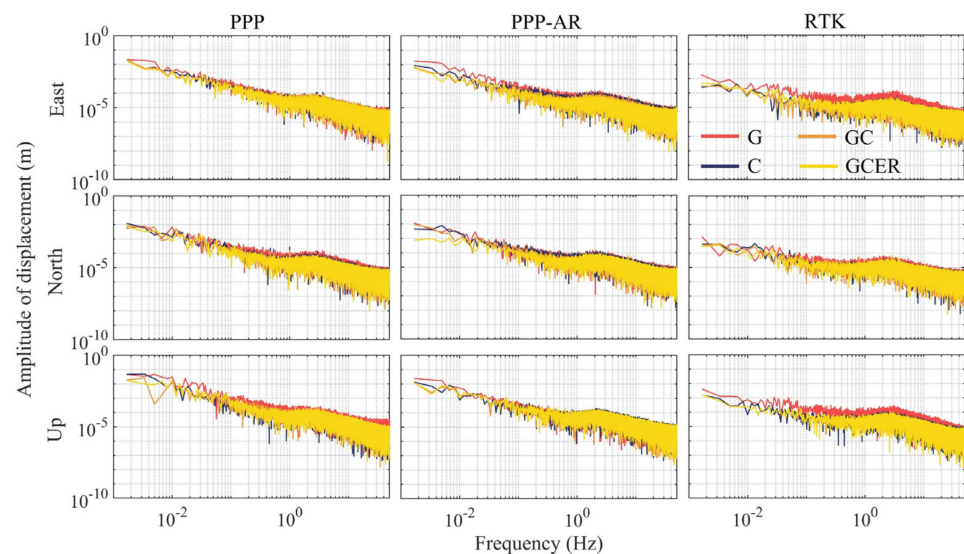
Figure 4. Amplitude–frequency spectra of 3D displacement results from G, C, GC, and GCER observations and PPP, PPP-AR, and RTK techniques in the stationary test. The upper, middle, and lower panels represent displacements in the East, North, and Up directions, respectively, while the left, middle, and right columns represent results from PPP, PPP-AR, and RTK, respectively.

3.2.2. Quasi-Static Motion Test

Figure 5 shows the 100-Hz displacement time series corresponding to the quasi-static motion test computed with the PPP, PPP-AR, and RTK techniques. Significant discrepancies can be seen among the different solutions. The GPS-only solutions have the lowest accuracy, with the RMSE value being 21.56 mm, 7.07 mm, and 6.51 mm for the PPP, PPP-AR, and RTK techniques, respectively. The BDS-only solutions show an improvement of up to 70% compared to the GPS-only solutions due mainly to the much smaller number of GPS satellites observed than that of BDS satellites (about 15 C and 5 G, Figure A2). The combined use of the GPS and BDS observations improved the accuracy by about 10% over the BDS-only solutions as judged by the RMSE value. When data from all four systems were used, the accuracy of the displacements was enhanced significantly for all three positioning techniques where the RTK technique achieved a sub-millimeter level of accuracy (RMSE = 0.75 mm), followed by the PPP-AR which allowed millimeter-level measurements of the quasi-static and abrupt motions.

The histograms of the displacement errors of the different processing techniques are shown in Figure 6 where the rows and columns represent the different processing techniques and the different combinations of GNSS observations, respectively. The range of the G and C solution errors from the PPP (first row in Figure 6) was from -4.62 to 2.27 cm, which was reduced significantly after the GC (-1.40–1.75 cm) and GCER (-0.83–1.48 cm) observations were used. The majority of the errors from the GCER observations were greater than 1 cm. When the PPP-AR technique was applied, the errors were reduced markedly to the range of -1.58–2.78 cm. The distribution pattern of the PPP-AR errors was similar to that of the PPP error; although, more errors were centered around 0 even for the GPS-only solutions. The GCER solutions achieved the best results with most of the errors within 1 cm. All the errors of the RTK results were within ±5 mm except for the GPS-only results that ranged between -0.40 and 1.40 cm.
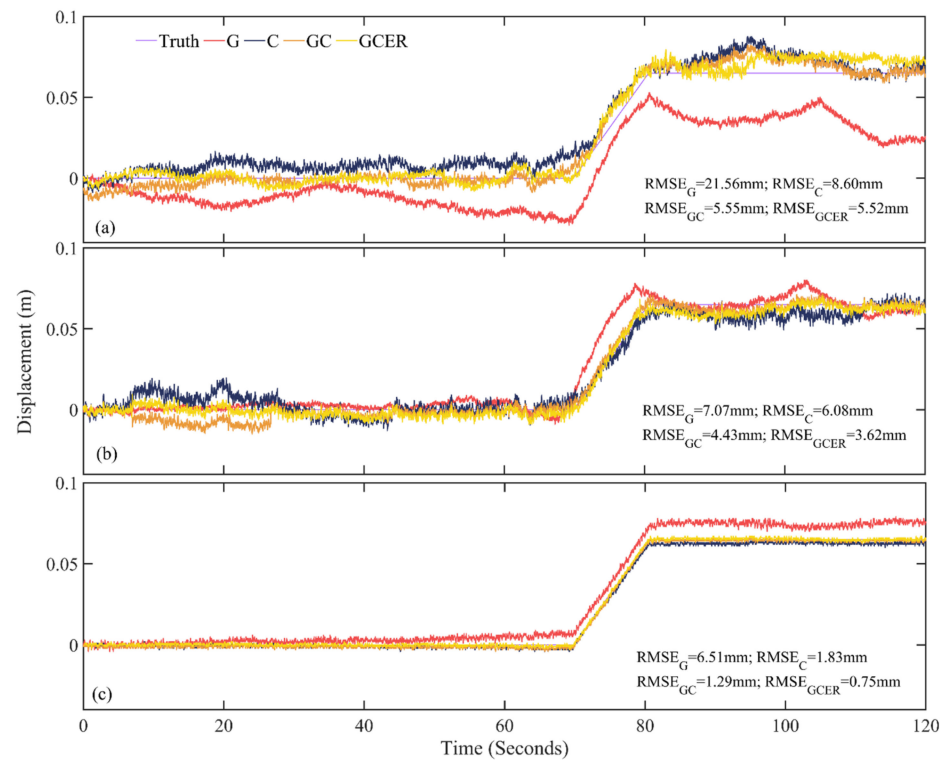
Figure 5. Displacement time series from the quasi-static motion test computed with observations from the different satellite systems and (**a**) PPP, (**b**) PPP-AR, (**c**) and RTK techniques (starting from 08:26:00 GPST).
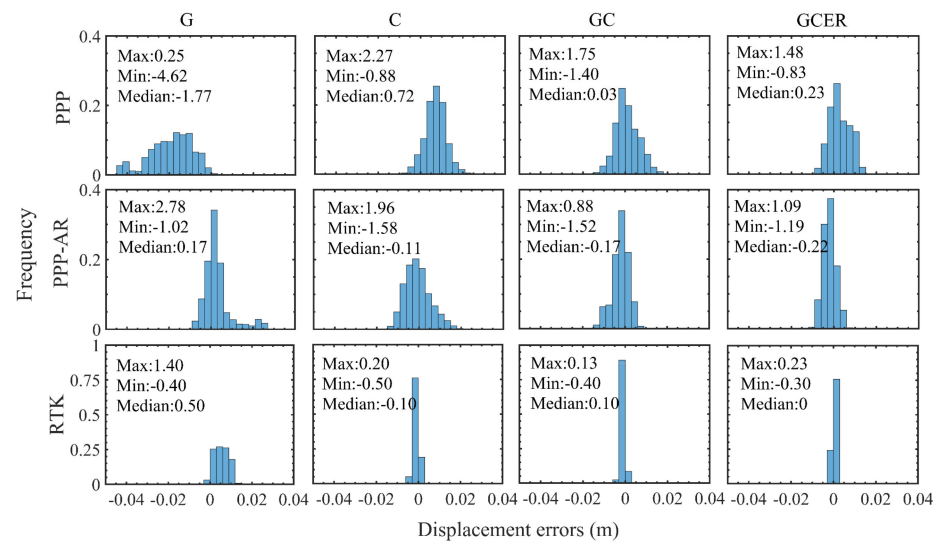

Figure 6. Histograms of displacement errors. From top to bottom, results from PPP, PPP-AR, and RTK; from left to right, results calculated by G, C, GC, and GCER, respectively. Statistics (maximum, minimum, and median) of each time series are given in each plot (in cm).

The amplitude–frequency spectra of the displacement errors from each positioning technique computed with Fast Fourier Transform (FFT) are shown in Figure 7 where the smaller amplitude indicates higher accuracy. The results indicate that the RTK results are more accurate than the other two positioning techniques, especially for those in the low-frequency band (less than 1 Hz). The displacement error spectra of PPP-AR are similar to that of PPP. The main discrepancies among different satellite system results are in the low-frequency band, where the GPS-only results have the worst performance for all positioning techniques due to limited

satellites. The results suggest that using the combination of the multi-GNSS observations could improve the displacement estimation performance effectively.
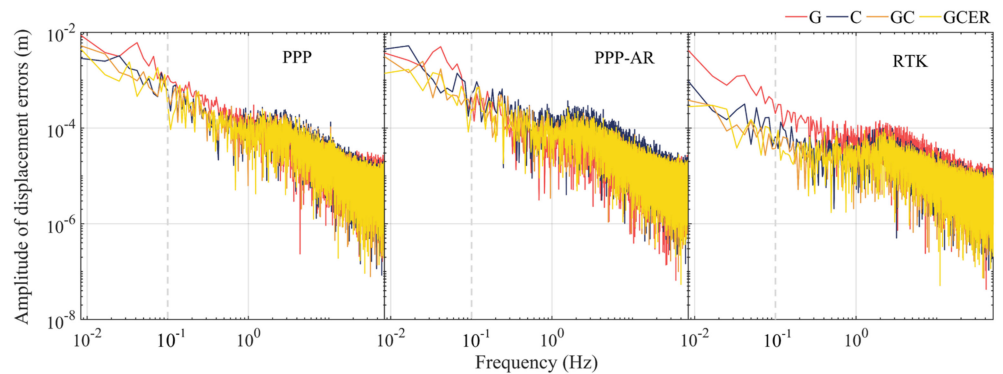
Figure 7. Amplitude–frequency spectra of displacement errors from quasi-static motion test computed with observations from the different satellite systems G, C, GC, and GCER, respectively. From left to right, results from PPP, PPP-AR, and RTK.

3.2.3. Sinusoidal Motion Test

As shown in Figure 2, a sinusoidal motion was simulated over three time periods. The motion had multiple vibration frequencies. Figure 8 shows the displacement times series from the different satellite systems and positioning techniques. The GPS-derived displacements from all the techniques are significantly biased due to the limited number of visible satellites, resulting in the RMSE being 4.59 cm, 3.60 cm, and 2.20 cm for PPP, PPP-AR, and RTK techniques, respectively. Similar to the quasi-static motion results, the BeiDou results were better than the GPS results due to much more satellites being tracked. Solutions from multi-GNSS observations (the last two rows in Figure 8) were improved noticeably compared to solutions from single satellite systems. A millimeter-level accuracy could be achieved with the RMSE of the solutions from the PPP, PPP-AR, and RTK techniques being 0.92 cm, 0.62 cm, and 0.35 cm, respectively.
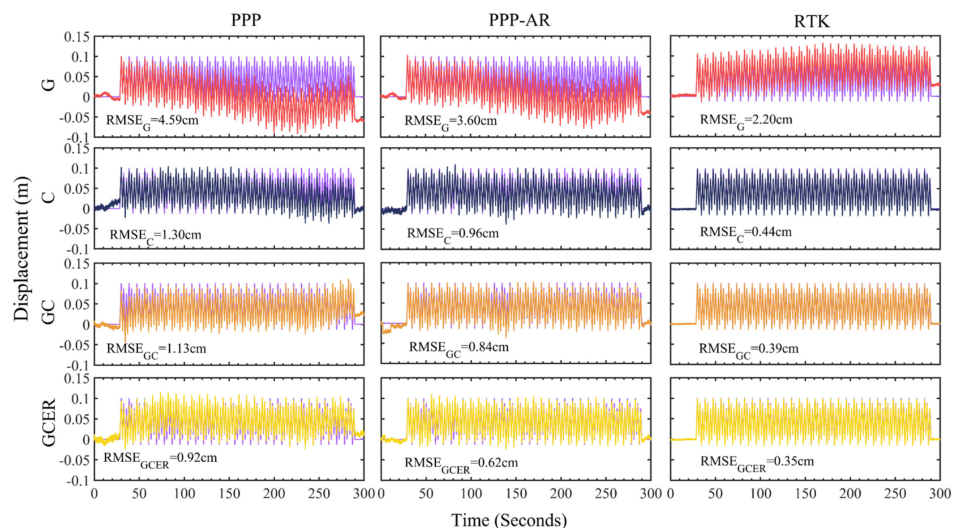

Figure 8. Sinusoidal displacement time series from the LDT (purple) and different satellite systems derived from (left column) PPP, (middle column) PPP-AR, and (right column) RTK techniques (starting from 08:32:00). From top to bottom, results, respectively, were computed from G (red), C (dark blue), GC (orange), and GCER (yellow) observations, respectively.

The histograms and spectra of the displacement errors from the different techniques are given in Figures 9 and 10, respectively. The displacement errors from PPP and GPS-only

observations distribute fairly evenly over the range of −8.71–1.20 cm, while a uni-modal structure centered around ±0.5 cm can be observed for displacement errors from Beidou-only and multi-GNSS observations. The distribution patterns of the errors from PPP-AR and PPP are similar, although the error ranges of the PPP-AR results are narrower. The errors of the RTK results concentrate much more around 0 except for the GPS-only solutions that have a bias.
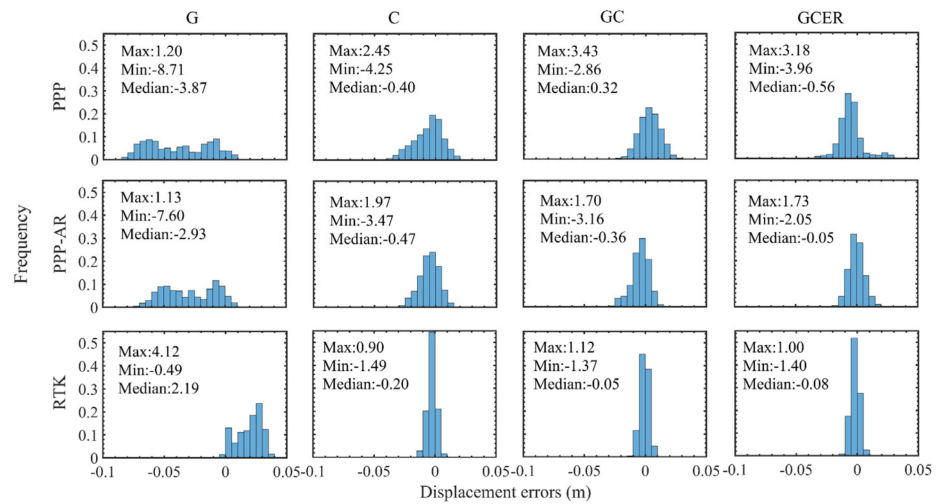
Figure 9. Histograms of displacement errors. From top to bottom, results correspond to PPP, PPP-AR, and RTK techniques while from left to right, results correspond to G, C, GC, and GCER observations, respectively. The maximum, minimum, and median values of each time series are given in each plot (in cm).
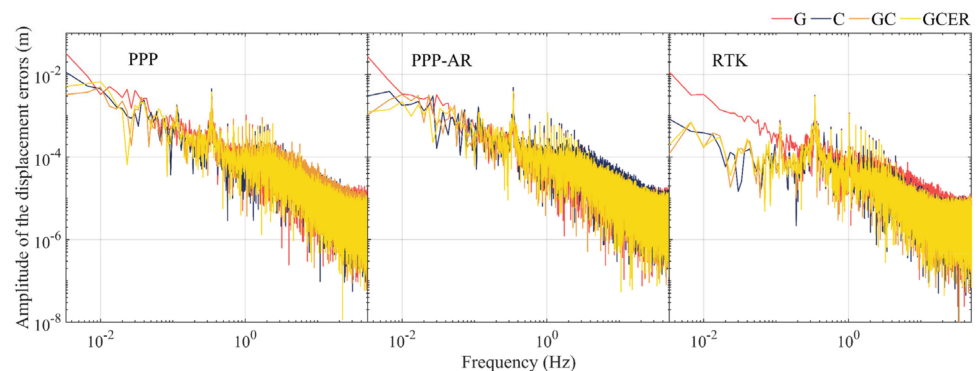

Figure 10. Amplitude–frequency spectra of displacement errors from sinusoidal motion test computed with observations from the different satellite systems G, C, GC, and GCER, respectively. From left to right, results from PPP, PPP-AR, and RTK.

The results in Figure 10 show the FFT spectra of the displacement errors. The RTK results have the best performance, especially for those in the low-frequency band (less than 1-Hz), followed by the PPP-AR technique. For different GNSS observation combinations, in terms of the low-frequency band, better results can be observed based on Beidou-only and multi-GNSS observations, while GPS-only solutions have the worst performance due to the biases (also see Figure 9). In addition, the results from different observations systems have similar accuracy in the high-frequency band.

The peak frequency and vibration amplitude of the results from each positioning technique computed with Fast Fourier Transform (FFT) are shown in Figure 11 and Table 2. The frequency and amplitude derived from the LDT solutions are regarded as benchmarks. The length and resolution of the FFT were 30,000 and 0.0033 Hz, respectively. The results indicate that the two peak frequencies could be well detected by all the positioning techniques, i.e., PPP, PPP-AR, and RTK; although, there are slight differences in the derived amplitudes.

The BeiDou-only results provided more accurate amplitude estimations than the GPS-only results, which is likely due to the BeiDou satellites being more available. The errors in the amplitudes estimated with RTK, PPP-AR, and PPP are within 0–0.3 mm, 0–0.6 mm, and 0.1–0.7 mm, respectively. In addition, the errors in the estimated amplitudes of the first peak are slightly larger than those in the second peak, which may be attributed to the fact that the second vibration frequency is more dominant and has a larger signal-to-noise ratio with respect to the first frequency [39].
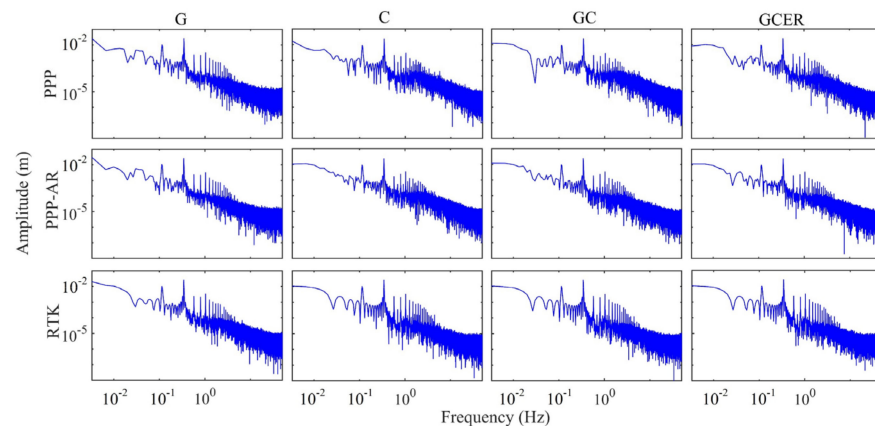
Figure 11. Amplitude–frequency spectra of displacement results from sinusoidal motion test. From top to bottom, results correspond to PPP, PPP-AR, and RTK techniques, while from left to right, results correspond to G, C, GC, and GCER observations (starting from 08:32:00 GPST).

Table 2. Peak frequencies and displacement amplitudes of the different data processing techniques. (in Hz and cm, respectively).

| GNSS System	1st Peak (Ref: 0.11/1.04)			2nd Peak (Ref: 0.34/2.68)		
	PPP	PPP-AR	RTK	PPP	PPP-AR	RTK
G	0.11/0.97	0.11/0.98	0.11/1.07	0.34/2.63	0.34/2.64	0.34/2.65
C	0.11/1.02	0.11/1.03	0.11/1.03	0.34/2.64	0.34/2.66	0.34/2.67
GC	0.11/0.99	0.11/0.99	0.11/1.05	0.34/2.66	0.34/2.69	0.34/2.67
GCER	0.11/1.00	0.11/1.02	0.11/1.04	0.34/2.69	0.34/2.68	0.34/2.68

3.3. Comparison of Displacement Results from Data of Different Sampling Rates

There has been a general understanding that high-sampling rate GNSS measurements may be noisier (e.g., [26]). We first tested data acquired when the antenna was stationary to study the accuracies of the displacement time series computed from data of different sampling rates. The 3D displacement time series are given in Figure 12 together with the standard deviations of the results. In general, the higher-rate results are slightly noisier; although, the differences are not very significant, and there are also some exceptions. The results indicate that PPP and PPP-AR are more sensitive to the increase in the sampling rate. There is also a bias that can be observed in the eastern and vertical PPP-AR results, in addition to noisier data for higher-rate observations. The possible reason is that high-rate observations not only contain white noise but also have relatively high levels of color noise [28], which may degrade the accuracy of the PPP-AR solutions [40]. There are not any noticeable differences in the RTK results.
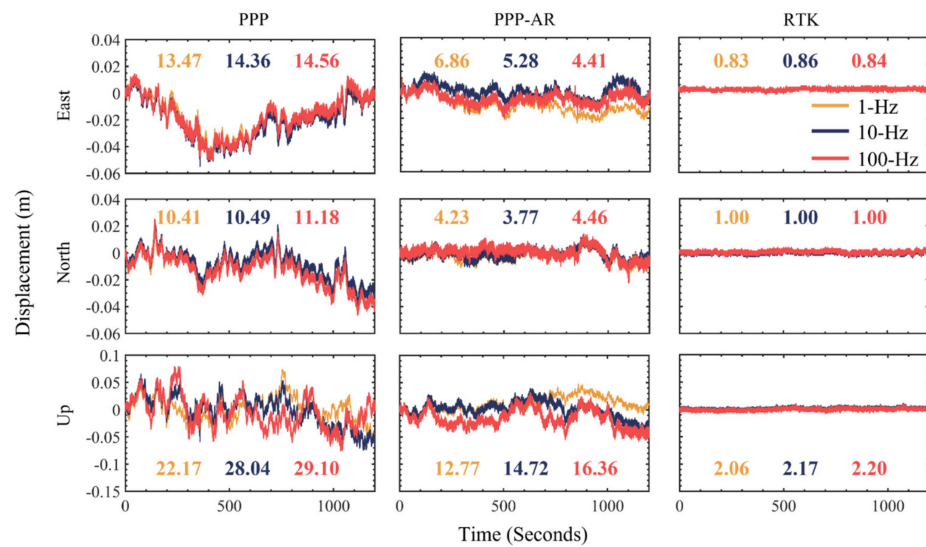
Figure 12. Three-dimensional displacement time series from multi-GNSS data of 100-, 10-, and 1-Hz, respectively, and PPP, PPP-AR, and RTK techniques. The upper, middle, and lower panels represent displacements in the East, North, and Up directions, respectively, while the left, middle, and right columns represent results from PPP, PPP-AR, and RTK, respectively. The standard deviation (in mm) of each time series is given in the corresponding color (Starting from 07:25:00 GPST).

The measured displacement time series when the antenna was in quasi-static and sinusoidal motions (starting from 08:26:00 (GPST) and lasting for 720 s) are shown in Figures 13 and A3. It can be seen from the results that the four simulated motion signals, starting at about 80 s and lasting about 570 s, can be clearly observable in all the results. Before testing the accuracies of the GNSS solutions with different sampling rates during the vibration period, we first validated whether there was any phase shift due to the time synchronization errors between the GNSS solutions and the LDT time series. Figures 14 and A5 show the 10-s comparison results between the GNSS and the LDT solutions from the different sampling rates, which are taken from the last two sinusoidal vibrations (also see Figure 13). In Figures 14 and A5, no obvious phase shift can be found between GNSS and LDT solutions for different sinusoidal oscillations.
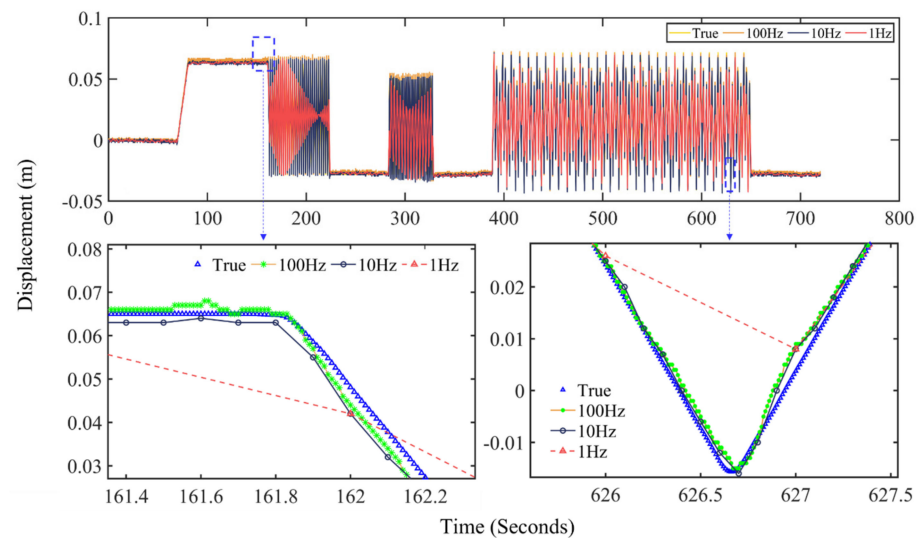
Figure 13. 100-Hz, 10-Hz, and 1-Hz displacement time series corresponding to quasi-static and sinusoidal motions derived from multi-GNSS observations and RTK technique (starting from 08:32:00 GPST).
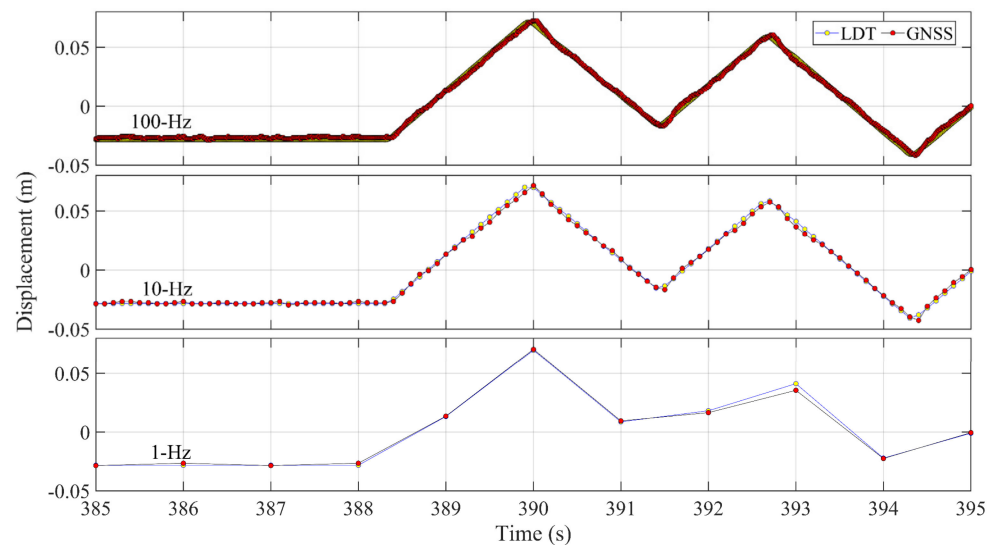
Figure 14. Comparison between 100-Hz, 10-Hz, and 1-Hz GNSS time series (red dots) and laser displacement transducer (yellow dots) for the third sinusoidal motion.

The RMSE of each of the time series in Figure 13 is given in Table 3. It is clear from the results that the higher the sampling rate is, the lower the accuracy. On average, the 10 Hz and 100 Hz results are 5.5% and 10.3% noisier than the 1 Hz results, respectively. Among the three positioning techniques, the accuracy of RTK is the highest and that of PPP is the lowest. The 1-Hz displacement results are significantly different in some parts of the time series, especially during the first two sinusoidal motion sections. This is considered due to the aliasing problem. The amplitude–frequency spectra of the first two sinusoidal motion sections calculated by the LDT solutions are shown in Figure A4. The peak frequencies of the two displacement signals were 0.50 Hz and 0.68 Hz, respectively, which could not be fully detected by the 1 Hz displacement series. Parts of the displacement time series were enlarged and shown in Figure 9b,c. The 10-Hz solutions were nearly the same as the 100-Hz solutions, although the 100-Hz solutions provided more detailed deformation. The advantage of 100 Hz solutions (i.e., the redundancy of data) is important in case of data filtering and data analysis, such as estimating the high-frequency parameters in certain loads (e.g., pre-dominant frequency of earthquakes loading [41] and accurate peak ground velocity in the near field [42]).

Table 3. RMSE of 100-, 10-, and 1-Hz displacement time series derived with PPP, PPP-AR, and RTK techniques (in mm). The values in the brackets are the percentage increases compared to the 1-Hz standard deviations.

Sampling Rate	PPP	PPP-AR	RTK
1-Hz	16.34	6.06	4.66
10-Hz	17.18 (5.1%)	6.58 (8.6%)	4.79 (2.8%)
100-Hz	17.96 (9.9%)	7.01 (15.6%)	4.91 (5.4%)

4. Conclusions

We have systematically assessed the performance of high-rate GNSS position observations computed with PPP, PPP-AR, and RTK techniques in monitoring structural deformation and dynamics based on a set of controlled experiments carried out in Hong Kong. When high-rate positioning was carried out, the RTK technique with observations from all the available GNSS offered the best accuracy among the tested positioning techniques and different combinations of satellite systems, followed by PPP-AR, which could potentially be an alternative approach to the commonly used RTK technique for millimeter-level SHM applications. The standard deviations of the 100 Hz GNSS displace-

ment solutions derived from PPP, PPP-AR, and RTK techniques were 5.5 mm, 3.6 mm, and 0.8 mm, respectively, when the antenna was in quasi-static motion, and were about 9.2 mm, 6.2 mm, and 3.5 mm, respectively, when the antenna was in vibration (up to about 0.7 Hz), under typical urban observational conditions in Hong Kong. We have also shown that the higher a sampling rate was, the lower the accuracy of a measured displacement series was. On average, the 10 Hz and 100 Hz results were 5.5% and 10.3% noisier than the 1 Hz results, respectively. However, since the high-rate data series offered more detailed displacement information, it is still critical to deploy the high-rate systems to monitor highly dynamic civil infrastructures despite the lower accuracy.

Appendix A

Figure A1. Location of the rover and the base stations.
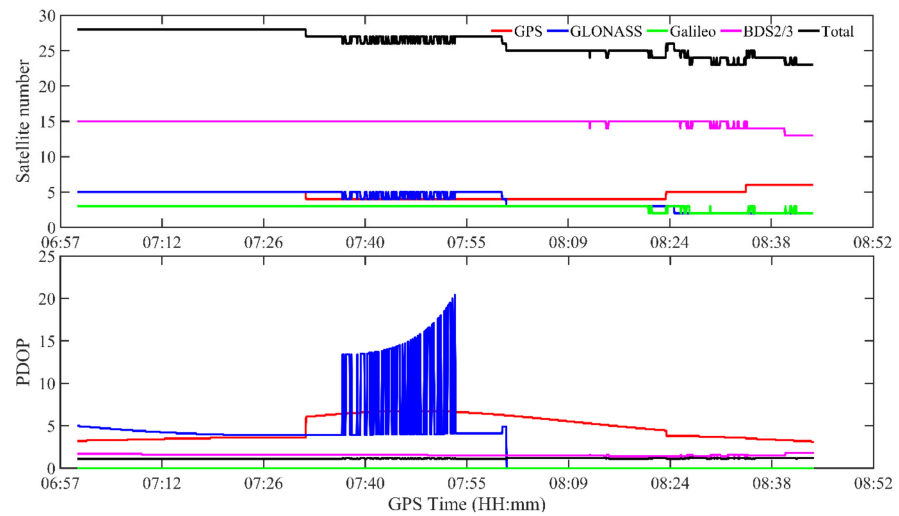
Figure A2. Satellite number (top) and Position Dilution of Precision (PDOP, bottom) during the experiment.
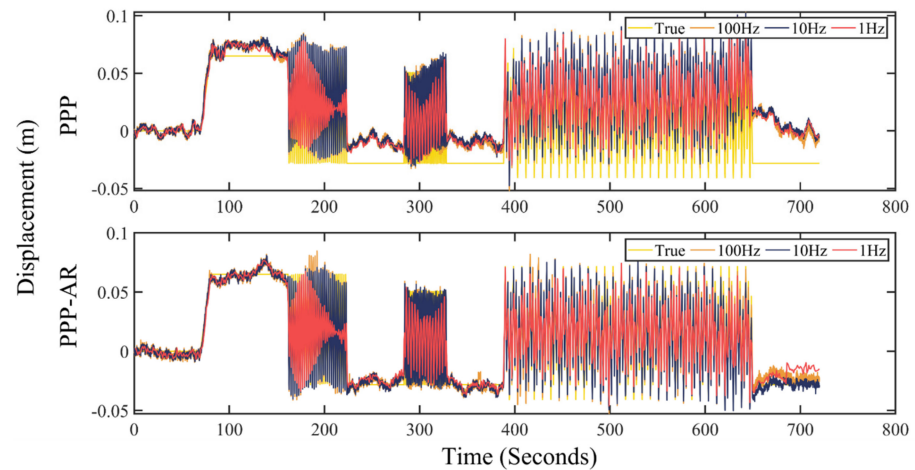
Figure A3. 100 Hz, 10 Hz and 1 Hz displacement time series corresponding to quasi-static and sinusoidal motion derived from multi-GNSS observations with PPP and PPP-AR techniques, respectively.
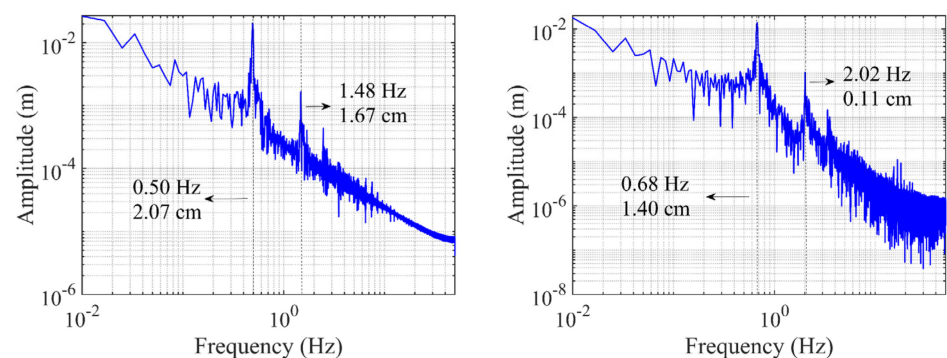
Figure A4. Amplitude-frequency spectra derived from the 100-Hz LDT data for the first (left) and second (right) sinusoidal motion sections.
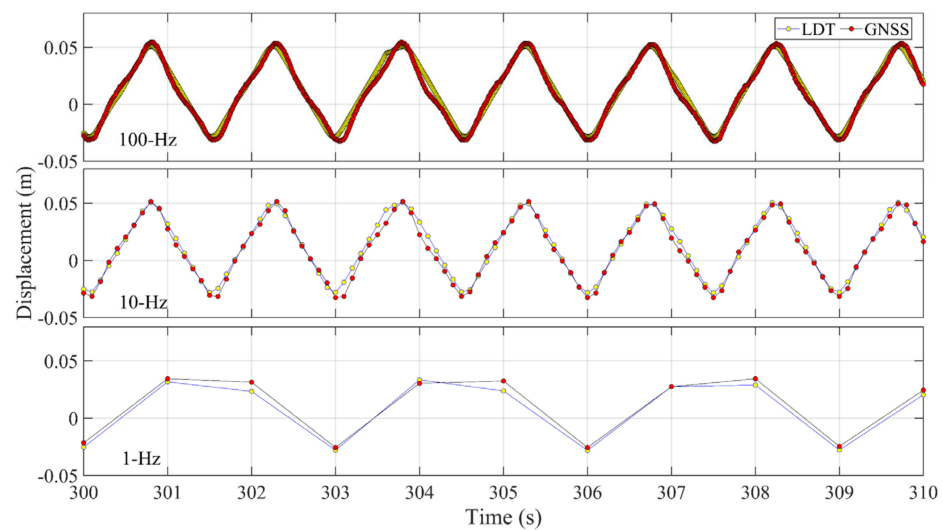
Figure A5. Comparison between 100-Hz, 10-Hz and 1-Hz GNSS time series (red dots) and laser displacement transducer (yellow dots) for the second sinusoidal motion.

References

1. Chan, W.S.; Xu, Y.L.; Ding, X.L.; Xiong, Y.L.; Dai, W.J. Assessment of dynamic measurement accuracy of GPS in three directions. *J. Surv. Eng.* **2006**, *132*, 108–117. [CrossRef]
2. Górski, P. Dynamic characteristic of tall industrial chimney estimated from GPS measurement and frequency domain decomposition. *Eng. Struct.* **2017**, *148*, 277–292. [CrossRef]
3. Xie, L.; Xu, W.; Ding, X. Precursory motion and deformation mechanism of the 2018 Xe Pian-Xe Namnoy dam Collapse, Laos: Insights from satellite radar interferometry. *Int. J. Appl. Earth Obs. Geoinf.* **2022**, *109*. [CrossRef]
4. Meng, X.; Wang, J.; Han, H. Optimal GPS/accelerometer integration algorithm for monitoring the vertical structural dynamics. *J. Appl. Geod.* **2014**, *8*, 265–272. [CrossRef]
5. Geng, J.; Pan, Y.; Li, X.; Guo, J.; Liu, J.; Chen, X.; Zhang, Y. Noise characteristics of high-rate multi-GNSS for subdaily crustal deformation monitoring. *J. Geophys. Res. Solid Earth* **2018**, *123*, 1987–2002. [CrossRef]
6. Zumberge, J.F.; Heflin, M.B.; Jefferson, D.C.; Watkins, M.M.; Webb, F.H. Precise point positioning for the efficient and robust analysis of GPS data from large networks. *J. Geophys. Res. Solid Earth* **1997**, *102*, 5005–5017. [CrossRef]
7. Zhong, P.; Ding, X.; Yuan, L.; Xu, Y.; Kwok, K.; Chen, Y. Sidereal filtering based on single differences for mitigating GPS multipath effects on short baselines. *J. Geod.* **2010**, *84*, 145–158. [CrossRef]
8. Chen, Q.; Jiang, W.; Meng, X.; Jiang, P.; Wang, K.; Xie, Y.; Ye, J. Vertical deformation monitoring of the suspension bridge tower using GNSS: A case study of the forth road bridge in the UK. *Remote Sens.* **2018**, *10*, 364. [CrossRef]
9. Dai, W.; Huang, D.; Cai, C. Multipath mitigation via component analysis methods for GPS dynamic deformation monitoring. *GPS Solut.* **2014**, *18*, 417–428. [CrossRef]
10. Xi, R.; Jiang, W.; Meng, X.; Chen, H.; Chen, Q. Bridge monitoring using BDS-RTK and GPS-RTK techniques. *Measurement* **2018**, *120*, 128–139. [CrossRef]
11. Xi, R.; Zhou, X.; Jiang, W.; Chen, Q. Simultaneous estimation of dam displacements and reservoir level variation from GPS measurements. *Measurement* **2018**, *122*, 247–256. [CrossRef]
12. Xu, P.; Shi, C.; Fang, R.; Liu, J.; Niu, X.; Zhang, Q.; Yanagidani, T. High-rate precise point positioning (PPP) to measure seismic wave motions: An experimental comparison of GPS PPP with inertial measurement units. *J. Geod.* **2013**, *87*, 361–372. [CrossRef]
13. Tang, X.; Liu, Z.; Roberts, G.W.; Hancock, C.M. PPP-derived tropospheric ZWD augmentation from local CORS network tested on bridge monitoring points. *Adv. Space Res.* **2022**, *69*, 3633–3643. [CrossRef]
14. Tu, R.; Wang, R.; Ge, M.; Walter, T.R.; Ramatschi, M.; Milkereit, C.; Dahm, T. Cost-effective monitoring of ground motion related to earthquakes, landslides, or volcanic activity by joint use of a single-frequency GPS and a MEMS accelerometer. *Geophys. Res. Lett.* **2013**, *40*, 3825–3829. [CrossRef]
15. Yigit, C.O.; El-Mowafy, A.; Anil Dindar, A.; Bezcioglu, M.; Tiryakioglu, I. Investigating Performance of high-rate GNSS-PPP and PPP-AR for structural health monitoring: Dynamic tests on shake table. *J. Surv. Eng.* **2021**, *147*, 05020011. [CrossRef]
16. Li, X.; Ge, M.; Zhang, X.; Zhang, Y.; Guo, B.; Wang, R.; Wickert, J. Real-time high-rate co-seismic displacement from ambiguity-fixed precise point positioning: Application to earthquake early warning. *Geophys. Res. Lett.* **2013**, *40*, 295–300. [CrossRef]
17. Yigit, C.O.; Gurlek, E. Experimental testing of high-rate GNSS precise point positioning (PPP) method for detecting dynamic vertical displacement response of engineering structures. *Geomat. Nat. Hazards Risk* **2017**, *8*, 893–904. [CrossRef]
18. Yu, W.; Peng, H.; Pan, L.; Dai, W.; Qu, X.; Ren, Z. Performance assessment of high-rate GPS/BDS precise point positioning for vibration monitoring based on shaking table tests. *Adv. Space Res.* **2022**, *69*, 2362–2375. [CrossRef]

19. Yu, J.; Meng, X.; Shao, X.; Yan, B.; Yang, L. Identification of dynamic displacements and modal frequencies of a medium-span suspension bridge using multimode GNSS processing. *Eng. Struct.* **2014**, *81*, 432–443. [CrossRef]

20. Moschas, F.; Avallone, A.; Saltogianni, V.; Stiros, S.C. Strong motion displacement waveforms using 10-Hz precise point positioning GPS: An assessment based on free oscillation experiments. *Earthq. Eng. Struct. Dyn.* **2014**, *43*, 1853–1866. [CrossRef]

21. Msaewe, H.A.; Psimoulis, P.A.; Hancock, C.M.; Roberts, G.W.; Bonenberg, L. Monitoring the response of Severn Suspension Bridge in the United Kingdom using multi-GNSS measurements. *Struct. Control. Health Monit.* **2021**, *28*, e2830. [CrossRef]

22. Cantieni, R. Transportation Research Board, National Research Council, Washington, DC, USA. In *Dynamic Load Testing of Highway Bridges*; National Research Council: Washington, DC, USA, 1984.

23. Kaloop, M.R.; Hu, J.W.; Elbeltagi, E. Adjustment and assessment of the measurements of low and high sampling frequencies of GPS real-time monitoring of structural movement. *ISPRS Int. J. Geo-Inf.* **2016**, *5*, 222. [CrossRef]

24. Yi, T.H.; Li, H.N.; Gu, M. Experimental assessment of high-rate GPS receivers for deformation monitoring of bridge. *Measurement* **2013**, *46*, 420–432. [CrossRef]

25. Moschas, F.; Stiros, S. Measurement of the dynamic displacements and of the modal frequencies of a short-span pedestrian bridge using GPS and an accelerometer. *Eng. Struct.* **2011**, *33*, 10–17. [CrossRef]

26. Moschas, F.; Stiros, S. PLL bandwidth and noise in 100 Hz GPS measurements. *GPS Solut.* **2015**, *19*, 173–185. [CrossRef]

27. Paziewski, J.; Sieradzki, R.; Baryla, R. Detection of structural vibration with high-rate precise point positioning: Case study results based on 100 Hz multi-GNSS observables and shake-table simulation. *Sensors* **2019**, *19*, 4832. [CrossRef]

28. Häberling, S.; Rothacher, M.; Zhang, Y.; Clinton, J.F.; Geiger, A. Assessment of high-rate GPS using a single-axis shake table. *J. Geod.* **2015**, *89*, 697–709. [CrossRef]

29. Shu, Y.; Fang, R.; Li, M.; Shi, C.; Li, M.; Liu, J. Very high-rate GPS for measuring dynamic seismic displacements without aliasing: Performance evaluation of the variometric approach. *GPS Solut.* **2018**, *22*, 121. [CrossRef]

30. Yang, Y.; Mao, Y.; Sun, B. Basic performance and future developments of BeiDou global navigation satellite system. *Satell. Navig.* **2020**, *1*, 1–8. [CrossRef]

31. Odolinski, R.; Teunissen, P.J. Best integer equivariant estimation: Performance analysis using real data collected by low-cost, single-and dual-frequency, multi-GNSS receivers for short-to long-baseline RTK positioning. *J. Geod.* **2020**, *94*, 1–17. [CrossRef]

32. Ge, M.; Gendt, G.; Rothacher, M.A.; Shi, C.; Liu, J. Resolution of GPS carrier-phase ambiguities in precise point positioning (PPP) with daily observations. *J. Geod.* **2008**, *82*, 389–399. [CrossRef]

33. Teunissen, P. The Least-Squares Ambiguity Decorrelation Adjustment: A Method for Fast GPS Ambiguity Estimation. *J. Geod.* **1999**, *73*, 587–593. [CrossRef]

34. Chan, W.S.; Xu, Y.L.; Ding, X.L.; Dai, W.J. An integrated GPS–accelerometer data processing technique for structural deformation monitoring. *J. Geod.* **2006**, *80*, 705–719. [CrossRef]

35. Zhang, Y.; Chen, J.; Gong, X.; Chen, Q. The update of BDS-2 TGD and its impact on positioning. *Adv. Space Res.* **2020**, *65*, 2645–2661. [CrossRef]

36. Montenbruck, O.; Steigenberger, P.; Prange, L.; Deng, Z.; Zhao, Q.; Perosanz, F.; Schaer, S. The Multi-GNSS Experiment (MGEX) of the International GNSS Service (IGS)–achievements, prospects and challenges. *Adv. Space Res.* **2017**, *59*, 1671–1697. [CrossRef]

37. Geng, J.; Chen, X.; Pan, Y.; Zhao, Q. A modified phase clock/bias model to improve PPP ambiguity resolution at Wuhan University. *J. Geod.* **2019**, *93*, 2053–2067. [CrossRef]

38. Böhm, J.; Möller, G.; Schindelegger, M.; Pain, G.; Weber, R. Development of an improved empirical model for slant delays in the troposphere (GPT2w). *GPS Solut.* **2015**, *19*, 433–441. [CrossRef]

39. Psimoulis, P.; Pytharouli, S.; Karambalis, D.; Stiros, S. Potential of Global Positioning System (GPS) to measure frequencies of oscillations of engineering structures. *J. Sound Vib.* **2008**, *318*, 606–623. [CrossRef]

40. Jiang, Y.; Gao, Y.; Zhou, P.; Gao, Y.; Huang, G. Real-time cascading PPP-WAR based on Kalman filter considering time-correlation. *J. Geod.* **2021**, *95*, 1–15. [CrossRef]

41. Psimoulis, P.A.; Houlié, N.; Behr, Y. Real-time magnitude characterization of large earthquakes using the predominant period derived from 1 Hz GPS data. *Geophys. Res. Lett.* **2018**, *45*, 517–526. [CrossRef]

42. Michel, C.; Kelevitz, K.; Houlié, N.; Edwards, B.; Psimoulis, P.; Su, Z.; Giardini, D. The potential of high-rate GPS for strong ground motion assessment. *Bull. Seismol. Soc. Am.* **2017**, *107*, 1849–1859. [CrossRef]